T2R2 東京科学大学 リサーチリポジトリ
Science Tokyo Research Repository

論文 / 著書情報
Article / Book Information

Title	Machine learning super-resolution of laboratory CT images in all-solid-state batteries using synchrotron radiation CT as training data
Authors	Manabu Kodama, Akihisa Takeuchi, Masamichi Uesugi, Shuichiro Hirai
Citation	Energy and AI, Vol. 14, 100305,
Pub. date	2023, 9
DOI	https://doi.org/10.1016/j.egyai.2023.100305
Creative Commons	Information is in the article.

Powered by T2R2 (Science Tokyo Research Repository)

Energy and AI 14 (2023) 100305

Contents lists available at ScienceDirect

Energy and AI

journal homepage: www.sciencedirect.com/journal/energy-and-ai

Machine learning super-resolution of laboratory CT images in all-solid-state batteries using synchrotron radiation CT as training data

M. Kodama [a,*], A. Takeuchi [b], M. Uesugi [b], S. Hirai [a]

[a] Tokyo Institute of Technology, 2-12-1 Ookayama, Meguro-ku, Tokyo 152-8550, Japan
[b] Japan Synchrotron Radiation Research Institute (JASRI/SPring-8), 1-1-1 Kouto, Sayo, Hyogo 679-5198, Japan

HIGHLIGHTS

- High-resolution X-ray CT imaging of all-solid-state batteries is discussed.
- Synchrotron radiation CT images offer higher resolutions than lab CT images.
- Super-resolution of lab CT achieved through machine learning.
- RED-Net+PReLU generates synchrotron-like high-resolution images from lab CT images.

GRAPHICAL ABSTRACT

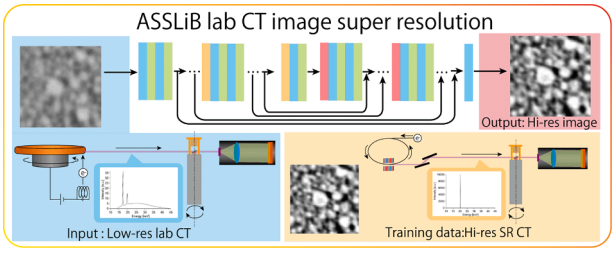

ARTICLE INFO

Keywords:
All-solid-state lithium-ion battery
X-ray CT
Laboratory CT
Synchrotron radiation CT
Super-resolution
Machine learning

ABSTRACT

High-performance all-solid-state lithium-ion batteries require observation, control, and optimization of the electrode structure. X-ray computational tomography (CT) is an effective nondestructive method for observing the electrode structure in three dimensions. However, the limited availability of synchrotron radiation CT, which offers high-resolution imaging with a high signal-to-noise ratio, makes it difficult to conduct experiments and restricts the use of X-ray CT in battery development. Conversely, laboratory CT systems are widely available, but they use X-rays emitted from a metal target, resulting in lower image quality and resolution compared with synchrotron radiation CT. This study explores a method for achieving comparable resolution in laboratory CT images of all-solid-state batteries to that of synchrotron radiation CT. Our method involves using the synchrotron radiation CT images as training data for machine learning super-resolution. The results demonstrate that, by employing an appropriate machine learning algorithm and activation function, along with a sufficiently deep network, the image quality of laboratory CT becomes equivalent to that of synchrotron radiation CT.

Introduction

The transition from gasoline to electric vehicles is being heavily promoted to reduce CO_2 emissions [1]. However, using conventional lithium-ion batteries causes both restricted driving range and slow charging, which hinder the widespread adoption of electric vehicles [2]. Fast charging decreases the concentration of lithium ions around the negative electrode, leading to overpotential and slow charging [3]. In addition, cooling mechanisms are necessary due to flammable organic electrolytes [4], which restrict the capacity and speed of electric vehicles. Solid-state lithium-ion batteries that use inorganic solid electrolytes are a potential solution [5]. Only the lithium-ion is transported in

* Corresponding author.
E-mail address: tanaka.m.ay@m.titech.ac.jp (M. Kodama).

https://doi.org/10.1016/j.egyai.2023.100305

Available online 25 September 2023
2666-5468/© 2023 The Author(s). Published by Elsevier Ltd. This is an open access article under the CC BY-NC-ND license (http://creativecommons.org/licenses/by-nc-nd/4.0/).

the solid electrolyte, enabling high-speed charging without the concentration over potential. Moreover, the solid electrolytes are thermally stable and, as a result, do not require cooling. Solid-state batteries can facilitate high-speed charging and the development of long-driving range electric vehicles.

Existing all-solid-state lithium-ion batteries have yet to achieve performance equal to or greater than conventional lithium-ion batteries using organic electrolytes. There are various reasons for this, but one is the insufficient optimization of the three-dimensional structure of the electrodes [6–11]. In conventional lithium-ion batteries, a sheet is created with gaps between the active material particles for storing lithium ions, and the liquid electrolyte is injected into this sheet. This ensures good contact between the active material and the electrolyte and enables the formation of an ion transport network within the electrode, resulting in high performance. In the case of all-solid-state lithium-ion batteries, the electrolyte is a solid (powder), making it impossible to create electrodes in a similar manner to existing lithium-ion batteries. Instead, the electrodes are created by preparing a mixture of the active material and solid electrolyte as a powder, and then pressing this mixture. However, forming a good interface between the active material and electrolyte or a good lithium transport network of electrolytes is more difficult than in conventional lithium-ion batteries using liquid organic electrolytes. For example, the aggregation of solid electrolyte particles can lead to the formation of a coarse network, increasing ion transport resistance within the electrode [6], while the aggregation of active material particles suppresses lithium diffusion within the active material, decreasing battery capacity [7]. Therefore, optimizing the electrode structure is vital in the practical application of all-solid-state batteries, and the development of electrode fabrication processes through detailed observations of the electrode structure is required. In particular, observations of the nano- and microscale three-dimensional fine structures inside all-solid-state batteries are necessary.

Several methods have been developed for structural observations of all-solid-state batteries, including focused ion beam scanning electron microscopy (FIB-SEM) [12], ultra-small-angle X-ray scattering (USAXS) [13], and X-ray computational tomography (CT) [6,7,11,14]. FIB-SEM involves repeated cross-sectional cutting and SEM observation, allowing for high-resolution three-dimensional observations down to the nanoscale [12]. However, as mentioned above, all-solid-state batteries are fabricated through compression molding, resulting in residual stress within the electrodes. This has led to concerns regarding the structural changes caused by stress release during cutting. USAXS is based on X-ray scattering, enabling nondestructive measurement of electrode structures. This technique has successfully measured the nanopore structure inside pressed solid electrolyte powders and is suitable for measuring nanoscale structures [13]. However, the output from these measurements is limited to statistical information about the structure, and the complete structural information required to discuss all aspects of battery performance in three dimensions cannot be provided. X-ray CT obtains a three-dimensional structure through a reconstruction process from a series of X-ray transmission images obtained while rotating the sample [15]. This measurement method overcomes the challenges of FIB-SEM and USAXS as it can acquire nondestructive three-dimensional structures.

There have been numerous structural observations of all-solid-state batteries using X-ray CT [6,7,11,14]. X-ray CT can be further classified into laboratory CT [16] and synchrotron radiation CT [17–19]. Both types obtain three-dimensional images by reconstruction from a series of X-ray transmission images, but they differ in the X-ray source used. Laboratory CT generates X-rays through electron collision with a metal target by accelerating thermally emitted electrons in a vacuum over a high-voltage range of 5–300 kV. X-rays can be emitted from compact devices with dimensions of less than 1 m; such devices are commonly found worldwide. However, the X-rays emitted from the metal target contain various wavelengths, and the intensity is weaker than that of synchrotron radiation CT. As a result, the contrast in the X-ray transmission images is relatively low, longer exposure times are required, and the signal-to-noise ratio (SNR) of the CT images is reduced. Synchrotron radiation CT generates X-rays by storing electrons accelerated to several GeV in a synchrotron storage ring and oscillating the stored electrons using an undulator. By using high-energy electron beams to generate X-rays, high-intensity X-rays are produced. When combined with a crystal monochromator, X-rays with excellent single-wavelength characteristics are generated. Using high-intensity and single-wavelength X-rays enables synchrotron radiation CT to capture images with high contrast and short exposure times. However, synchrotron radiation CT systems are large-scale devices (typical dimensions on the kilometer scale), and there are only a few such systems worldwide. Synchrotron radiation CT systems capable of observing all-solid-state battery electrodes containing heavy metals such as cobalt using hard X-rays are limited to very few facilities, such as SPring-8 [18] and NSLS [19].

Synchrotron radiation CT can achieve high-resolution imaging even with the same voxel size as laboratory CT [20]. As mentioned above, this is because of their high-intensity X-rays with excellent single-wavelength characteristics, which result in CT images with a high SNR and increased effective resolution. However, the limited availability of synchrotron radiation CT systems makes it difficult to use them for battery development. Obtaining laboratory CT images with an equivalent high effective resolution to synchrotron radiation CT would facilitate the optimization of electrode structures in all-solid-state batteries and promote their high-performance development.

In recent years, research on super-resolution, which enhances the resolution of an image using machine learning techniques, has been actively conducted [21]. This approach involves training a neural network using high-resolution images as the training data, and then supplying low-resolution images as the input and generating high-resolution images as the output. Various network architectures, such as the Super-Resolution Convolutional Neural Network (SRCNN) [22], which can achieve super-resolution with a simple network structure, and Residual Encoder-Decoder Network (RED-Net) [23], which can achieve high-accuracy super-resolution by suppressing gradient loss through skip connection, have been proposed, and machine learning has been shown to be an effective method for super-resolution in numerous studies. Super-resolution technique of CT images with machine learning has been explored. Dreier et al. have successfully employed machine learning to enhance CT images captured in low-resolution mode of organic materials' laboratory CT to achieve resolution comparable to those captured in high-resolution mode [24]. Similarly, Omori et al. have realized super-resolution for CT images of rock samples [25]. However, these studies need to improve in achieving resolutions beyond that of the laboratory CT images when using laboratory CT as the training data. To achieve resolutions surpassing those of laboratory CT through super resolution, it would be necessary to employ machine learning with synchrotron radiation CT, which inherently holds a potentially higher resolution than laboratory CT. Nevertheless, no prior research examples exist in this context. The application of machine learning-based super-resolution techniques trained by synchrotron radiation CT has the potential to achieve an equivalent effective resolution in laboratory CT images as provided by synchrotron radiation CT images.

Motivated by the above discussion, this study attempted to achieve super-resolution of laboratory CT images using machine learning, with laboratory CT images as the input and synchrotron radiation CT images as the training data. The imaging target was the all-solid-state lithium-ion battery cathode with an electrolyte material of LPS glass and an active material of lithium cobalt oxide ($LiCoO_2$). Initially, a comparison was made between laboratory CT images and synchrotron radiation CT images of the all-solid-state lithium-ion battery cathode. Subsequently, a search was conducted to find an appropriate network architecture and activation function to achieve super-resolution of laboratory CT images using synchrotron radiation CT images as the training data. As a result,

laboratory CT images with an equivalent effective resolution to that of synchrotron radiation CT were obtained through super-resolution. These findings are reported in the present paper.

Experimental and machine learning procedures

In this study, we created a cathode for a representative all-solid-state battery using LPS glass as the solid electrolyte and $LiCoO_2$ as the active material. After punching the electrode using a hand punch, it was enclosed in a CT imaging jig for sealing, and CT imaging experiments were conducted. The CT imaging was performed using both a laboratory CT system and a synchrotron radiation CT system. Subsequently, the obtained CT images were subjected to a machine learning-based super-resolution technique to enhance the resolution of the laboratory CT images, with the synchrotron radiation CT images used as training data.

Experimental procedures

All-solid-state battery electrode for CT measurements

An electrode for a representative all-solid-state battery cathode suitable for X-ray CT imaging was fabricated using LPS glass [26] as the solid electrolyte and $LiCoO_2$ as the active material. The LPS glass was synthesized from Li_2S (99.98 %, Sigma-Aldrich) and P_2S_5 (99 %, Merck). The Li_2S and P_2S_5 were mixed at a Li_2S-to-P_2S_5 ratio of 75:25 in an agate mortar. The resulting mixed powder (3 g) was sealed in a 50-ml zirconia pot along with ten zirconia balls of diameter 10 mm, ten zirconia balls of diameter 5 mm, and a grinding aid (0.2 ml of diethyl ether). Mechanical milling was performed at 300 rpm for 10 h by a planetary boll mill (Ito Seisakusho, LP-M2) with a rotation ratio of 2:1 to synthesize the LPS glass.

The obtained LPS glass was mixed with $LiCoO_2$ to create the electrode composite material. $LiCoO_2$ with an average particle size of 5 μm was mixed at a $LiCoO_2$-to-LPS glass volume ratio of 70:30. The weighed $LiCoO_2$ was sealed in a 50-ml zirconia pot with 30 g of zirconia balls (φ1 mm) and mixed for 1 h using a rolling mill (AV-1, Asahi Rika Seisakujo) to obtain the electrode composite material.

The obtained composite material was placed in a φ5 mm pellet die and pressed at 200 MPa using a hydraulic press to create a cathode with a thickness of 100 μm. The resulting cathode was punched using a hand punch (NOGAMI) to a diameter of 0.3 mm, and this was used as the sample for CT imaging. The sample size had a diameter of 0.3 mm to ensure sufficient X-ray transmission in the laboratory CT. The φ0.3 mm CT imaging sample was enclosed in a CT imaging jig with a low-dew-point internal condition (<−80 °Cdp) to suppress the degradation and transformation of LPS glass in the electrode caused by moisture [7]. The entire sequence of operations for material synthesis, mixing, pressing, and loading into the jig was conducted inside a purged glove box (Miwa) filled with low-dew-point argon (<−80 °Cdp).

Laboratory X-ray CT measurements

The laboratory CT imaging was performed using the nano 3DX (Rigaku). Fig. 1(a) shows a schematic diagram of the laboratory CT system. Thermal electrons generated from the filament were accelerated and collided with a molybdenum electrode at an accelerating voltage of 44 kV, resulting in the generation of X-rays through the reverse-Compton effect. The molybdenum electrode was employed in the rotating anode mode, allowing for variations in the irradiated area by the electron beam, thus suppressing molybdenum depletion from heat and enabling stable X-ray irradiation. The emitted X-ray spectrum, shown in the center of Fig. 1(a), exhibits peaks at 17.4 and 19.6 keV corresponding to the molybdenum Kα and Kβ lines, as well as a broad spectrum of continuous X-rays with a maximum of around 25 keV. These X-rays were irradiated into the sample in the CT imaging jig, and the transmitted X-rays were converted into visible light by a scintillator. The transmitted images were then magnified and projected onto an imaging sensor using a microscope, capturing the transmitted images. The pixel size of the transmitted images was 310 nm. Each transmitted image was acquired with a 30-s exposure, and the sample was rotated by 180° in increments of 1000 steps to obtain a series of transmitted images. The total imaging time was 500 min. The CT images were reconstructed from the series of transmitted images, and the voxel size of the CT images was 310 nm × 310 nm × 310 nm.

Synchrotron radiation X-ray CT measurements

Synchrotron radiation X-ray CT imaging was performed using the micro-CT system in the BL20XU beamline of the large-scale SPring-8 synchrotron facility [27]. Fig. 1(b) shows a schematic diagram of the system. Electrons were accelerated up to 8 GeV and introduced into the

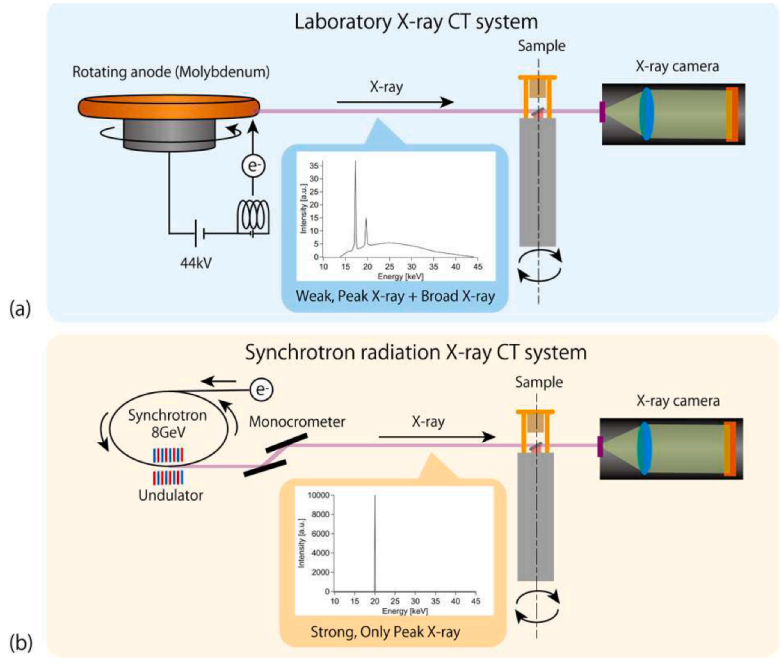

Fig. 1. Schematics of (a) laboratory X-ray CT system and (b) synchrotron radiation X-ray CT system.

storage ring, where a current of 100 mA was maintained at 8 GeV. X-rays were emitted by oscillating the electrons using an undulator installed in the storage ring. The emitted X-rays passed through a monochromator consisting of opposing silicone single-crystal plates cooled by liquid nitrogen, allowing only 20 keV X-rays to be extracted. These X-rays were irradiated onto the sample in the CT imaging jig. The transmitted X-rays were converted into visible light by a scintillator, similar to the laboratory CT system, and then magnified and projected onto an image sensor to obtain the transmitted images. The pixel size of the transmitted images was 495 nm. The difference in pixel size between laboratory CT and synchrotron radiation CT is due to using different X-ray sources, each with optimized optics and cameras. Each transmitted image was acquired with a 50-ms exposure, and the sample was rotated by 180° in increments of 1000 steps to obtain a series of transmitted images. The total imaging time was 1 min. The CT images were reconstructed from the series of transmitted images, and the voxel size of the CT images was 495 nm × 495 nm × 495 nm.

Machine learning procedures

The super-resolution of laboratory CT images was achieved using machine learning with synchrotron radiation CT images as the training data. Because of the different voxel sizes in the laboratory CT (310 nm × 310 nm × 310 nm) and synchrotron radiation CT (495 nm × 495 nm × 495 nm), the voxel size of all CT images was standardized to 600 nm × 600 nm × 600 nm using linear interpolation. The voxel size of 600 nm × 600 nm × 600 nm was selected to minimize the effective resolution reduction due to linear interpolation while keeping the memory size within the range feasible on a consumer GPU. Fig. 2 shows the laboratory and synchrotron radiation CT images before and after linear interpolation. The image quality degradation of synchrotron radiation CT image due to linear interpolation is negligibly slight. The converted CT images had a size of 512 × 512 × 200 voxels. Although CT images are three-dimensional, directly applying super-resolution to the three-dimensional images would result in massive amounts of data and network sizes that cannot be processed with commercially available GPUs. Therefore, super-resolution processing was performed on the 512 × 512 two-dimensional cross-sectional images obtained by slicing the 3D images. Of the 200 cross-sectional CT images, 180 were used as training data and the remaining 20 were used as validation data. The images produced by the machine learning technique correspond to the validation data. The Neural Network Console (Sony) machine learning

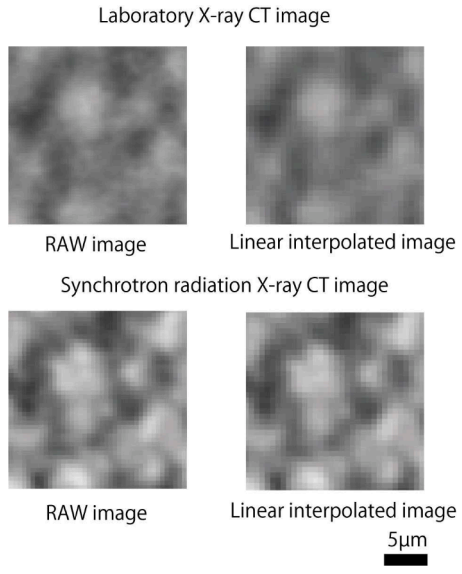

Fig. 2. Laboratory and synchrotron radiation CT images of raw image and after the linear interpolation.

software was used, and each network described in this paper was trained for 2000 epochs. The calculations were performed using GeForce RTX 4090 (Nvidia) GPUs. The SRCNN [22] and RED-Net [23] networks were employed. Since the ReLU function is used in the SRCNN and Red-NET proposing studies, in this paper, the ReLU [28] activation function was used unless otherwise specified.

Fig. 3 shows the structures of the neural networks used in this study. Both are convolutional neural networks that connect convolutional layers with activation functions. SRCNN sequentially connects convolutional layers and activation functions. Increasing the depth of the SRCNN involves inserting additional layers in the feature extraction network. In contrast, RED-Net consists of an encoder and a decoder, with MaxPooling and UnPooling layers used to change the resolution and incorporate skip connections.

The similarity between the data obtained by super-resolution of laboratory CT images using machine learning and synchrotron radiation CT images was evaluated using the peak SNR (PSNR). The PSNR was calculated using the ImageMagick image analysis software. The PSNR measures the similarity between images and is expressed in dB. Higher PSNR values indicate a higher degree of similarity between images. In this study, a higher PSNR indicates successful super-resolution of the laboratory CT images.

Results and discussion

This section compares laboratory CT images and synchrotron radiation CT images of an all-solid-state battery cathode to investigate their respective imaging characteristics. Subsequently, the super-resolution of laboratory CT is performed using machine learning with SRCNN and RED-Net, with the synchrotron radiation CT images serving as training data. The super-resolution characteristics of each method and the techniques employed to achieve satisfactory super-resolution are then discussed.

Comparison of laboratory X-ray CT images and synchrotron radiation X-ray CT images

Fig. 4 shows a laboratory CT image (Fig. 4(a)) and a synchrotron radiation CT image (Fig. 4(b)) of the same region of an all-solid-state battery cathode. The left-hand images in each panel represent the overall view, while the right-hand panels display an enlarged image. The all-solid-state battery cathode consists of three components: cathode active material, solid electrolyte, and voids. Among these, the active material (with the highest X-ray absorption rate) appears as a bright white region, the solid electrolyte (with an intermediate X-ray absorption rate) appears as a gray region, and the voids (with a low X-ray absorption rate) appear as black regions in the CT images.

By comparing the overall views (left-hand panels of Fig. 4(a) and (b)), it is evident that the synchrotron radiation CT exhibits higher contrast than the laboratory CT. The PSNR of the laboratory CT image to the synchrotron radiation CT image is 12.8 dB. This value reflects the significant degradation of image quality in the laboratory CT compared with the synchrotron radiation CT [29]. As mentioned earlier, this is because the synchrotron radiation CT uses highly monochromatic X-rays generated by an undulator and a monochromator, enabling the clear output of X-ray absorption rates of the sample as brightness in the CT images. When comparing the details (right-hand panels of Fig. 4(a) and (b)), the higher contrast of synchrotron radiation CT compared with laboratory CT is clear, similar to the overall views. However, in the laboratory CT, the image appears blurry, making it difficult to observe fine structures on the order of 1 μm, whereas synchrotron radiation CT captures these fine structures. Despite the voxel size during acquisition being smaller in the laboratory CT (310 nm × 310 nm × 310 nm) than in the synchrotron radiation CT (495 nm × 495 nm × 495 nm), the latter has a better ability to capture detailed structures. This is attributable to the use of high-intensity X-rays in synchrotron CT, which allows for the

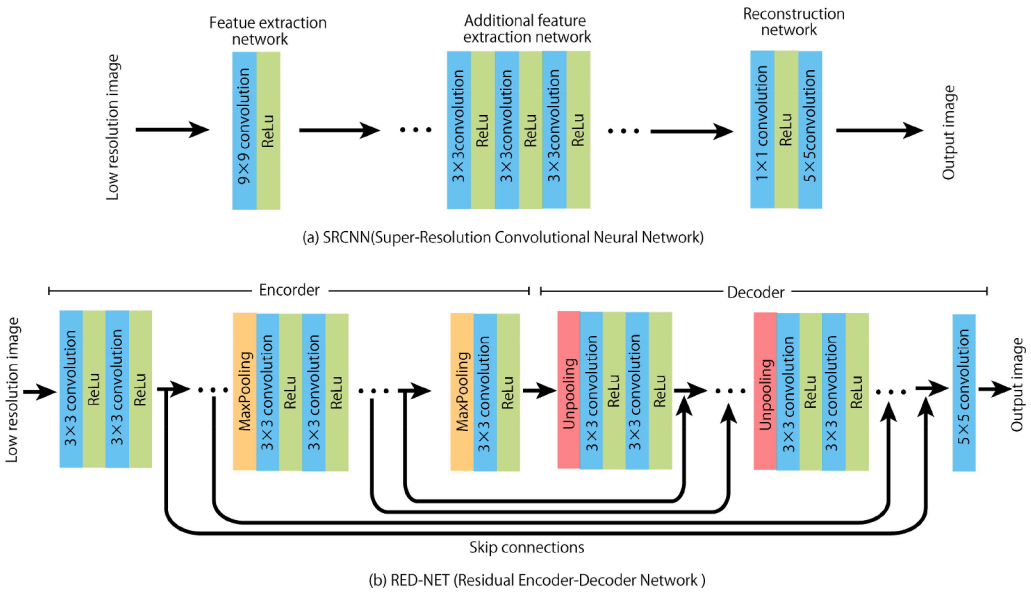

Fig. 3. Convolutional neural networks for super-resolution used in this study: (a) SRCNN, (b) RED-NET.

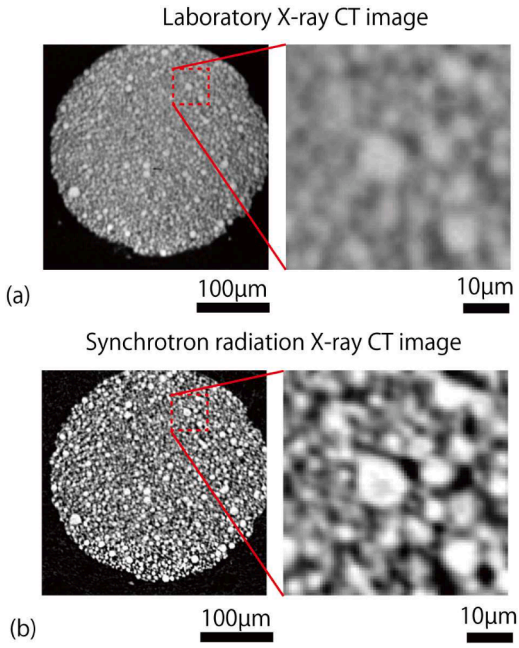

Fig. 4. X-ray CT image of all-solid-state battery cathode with (a) laboratory X-ray CT system and (b) synchrotron radiation X-ray CT system.

acquisition of transmission images with a high SNR for CT reconstruction, resulting in CT images with high SNR. The shorter acquisition time of synchrotron radiation CT (1 min) compared with laboratory CT (500 min) reduces the sample displacement caused by temperature changes during imaging, leading to a reduction in drift artifacts [30].

Super-resolution with SRCNN

Fig. 5 illustrates the laboratory CT image (Fig. 5(a), Lab. CT), the laboratory CT image after super-resolution using SRCNN (Fig. 5(b)–(e)), and the synchrotron radiation CT image (Fig. 5(f), S.R. CT). For each laboratory CT image and super-resolution processed image, the PSNR with respect to the synchrotron radiation CT image is indicated. In this figure, only the enlarged images from the right-hand column of Fig. 4 are shown.

As mentioned in the previous section, the laboratory CT image has a lower resolution than the synchrotron radiation CT, with a PSNR of 12.8 dB. When super-resolution is applied using the SRCNN without additional networks, as shown in Fig. 5(b), there is some improvement in contrast, but fine structures (<1 μm) cannot be restored, resulting in a PSNR of 15.6 dB. This means that the SRCNN failed feature extraction. Even with the addition of layers to the network, enabling more complex image processing (Fig. 5(c)–(e)), these fine structures are not restored. Moreover, the contrast decreases because of the additional network layers, resulting in a PSNR of less than 15.6 dB. Adding layers to the network increases the complexity of potential processing. However, the SRCNN failed the fracture extraction without the additional networks, and the learning efficiency decreases as the number of parameters grows. As a result, the absence of additional networks yields the highest

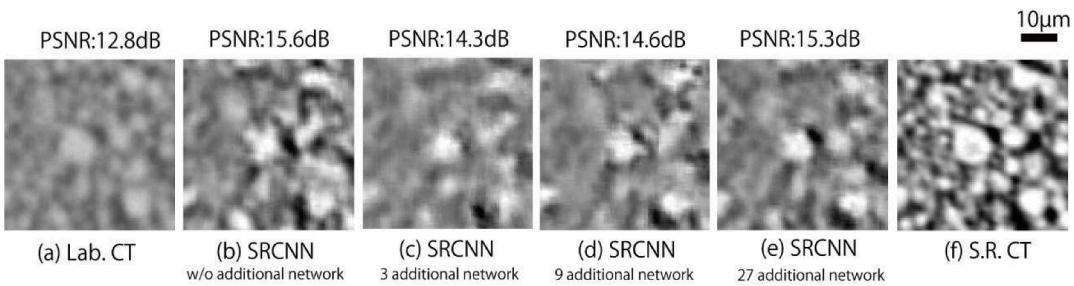

Fig. 5. Super-resolution of laboratory X-ray CT image by SRCNN.

PSNR. The reason for the failure of the feature extraction in SRCNN would be that the current dataset of training data (180 CT slice images) might not be enough to achieve super-resolution using SRCNN. The best way to increase the super-resolution accuracy is to increase the amount of the training dataset. However, as mentioned in the introduction, there are only a few high-performance synchrotron radiation facilities worldwide, and it is challenging to obtain sufficient teacher data. One possible approach is introducing pre-training into the SRCNN, which may improve super-resolution accuracy even with a small amount of training data.

Super-resolution with RED-Net

Fig. 6 shows the laboratory CT image (Fig. 6(a)), the super-resolution laboratory CT image processed using RED-Net (Fig. 6(b)–(f)), and the synchrotron radiation CT image (Fig. 6(g)). Similar to Fig. 5, the PSNR values with respect to the synchrotron radiation CT image are indicated above each image, and only the enlarged images from the right-hand column of Fig. 4 are shown. The super-resolution achieved by RED-Net, which consists of a three-layer encoder and decoder and processes images from 512 × 512 pixels down to 128 × 128 pixels for coarse-graining, is shown in Fig. 6(b). The contrast improvement is similar to that of SRCNN (Fig. 5(b)), with a PSNR of 15.6 dB. Increasing the network depth from three layers to six layers results in the restoration of finer detail, as shown in Fig. 6(b)–(e), improving the PSNR to 22.4 dB. However, deepening the network structure to seven layers (Fig. 6(f)) produces an image similar to that of the six-layer case (Fig. 6(e)), and the PSNR decreases to 22.1 dB. Processing up to seven layers effectively coarse-grains the image to 8 × 8 pixels. In this case, although a global structure is extracted, the battery does not have such large-scale structures. Therefore, deepening the network structure to seven layers does not effectively extract more features, resulting in a similar processing outcome to that of the six-layer case.

For the image segmentation of the all-solid-state battery cathode CT images using U-Net, the PReLU activation function results in better accuracy than the ReLU function [31]. PReLU is an activation function with a gradient in the negative region, addressing the issue of output values and gradients becoming zero with ReLU, which can lead to learning stagnation [32]. Given the similarity in structure between RED-Net and U-Net, switching the activation function from ReLU to PReLU in RED-Net with a six-layer network structure has the potential to achieve higher-accuracy super-resolution. Fig. 7 shows the laboratory CT image (Fig. 7(a)), synchrotron radiation CT image (Fig. 7(b)), the super-resolution laboratory CT image processed using RED-Net with the ReLU activation function (Fig. 7(c)), and the super-resolution laboratory CT image processed using RED-Net with the PReLU activation function (Fig. 7(d)). Although the image processed with the ReLU function (Fig. 7(c)) reproduces fine structures to some extent, there are slight differences in fine structure compared with the synchrotron radiation CT image (Fig. 7(b)). However, the image processed with the PReLU function (Fig. 7(d)) closely resembles the synchrotron radiation CT image, and it is difficult to distinguish any differences. In this case, the PSNR value exceeds 30 dB. Considering that a PSNR of 30 dB or above is generally acceptable in CT images [29], it can be concluded that practical super-resolution can be achieved using RED-Net with the PReLU activation function.

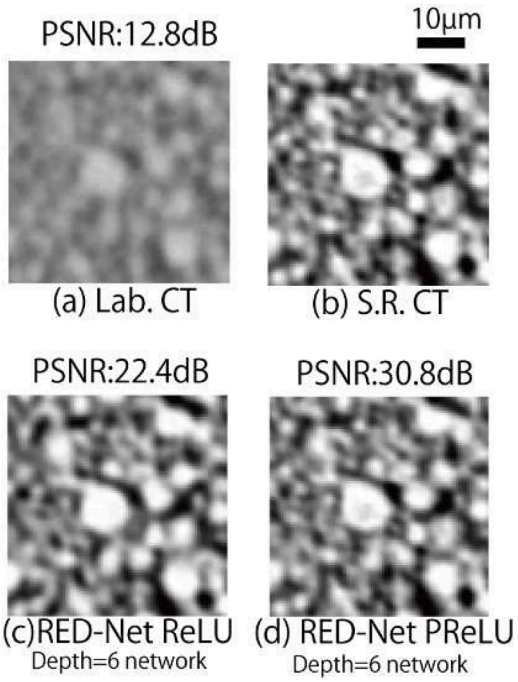

Fig. 7. Super-resolution of laboratory X-ray CT image by RED-Net with ReLU and PReLU.

Finally, Fig. 8 shows the overall view of the experimental laboratory CT image (Fig. 8(a)), the super-resolution laboratory CT image processed by RED-Net with PReLU (Fig. 8(b)), and the synchrotron radiation CT image (Fig. 8(c)) of various CT images. While Fig. 7 provided a detailed verification using enlarged images, Fig. 8 demonstrates that RED-Net with PReLU produces satisfactory images in terms of the overall view. At this scale, distinguishing between the super-resolution images processed by RED-Net with PReLU (Fig. 8(b)) and the synchrotron radiation CT image (Fig. 8(c)) becomes extremely difficult.

From the results presented above, it is evident that machine learning-based super-resolution of laboratory CT images using RED-Net with PReLU, guided by synchrotron radiation CT, produces high-resolution images from laboratory CT that are comparable to those of synchrotron radiation CT.

Conclusions

Nondestructive high-resolution 3D structural measurements of all-solid-state lithium-ion batteries can be achieved using synchrotron radiation CT, which generates high-energy and single-wavelength beams. However, the number of synchrotron radiation CT systems capable of such measurements is limited, imposing constraints on their active use in battery research. Although laboratory X-ray CT systems are widely available, they suffer from the weak and multi-wavelength

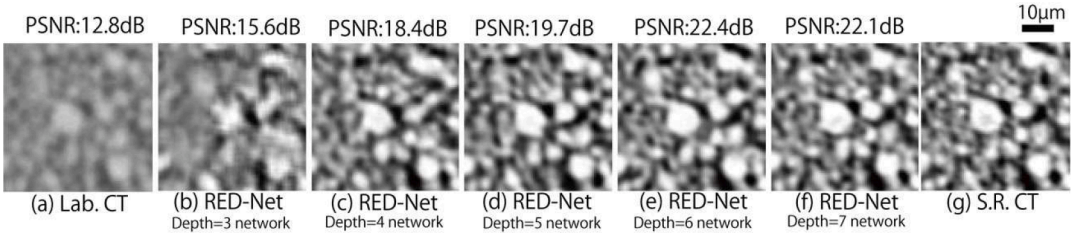

Fig. 6. Super-resolution of laboratory X-ray CT image by RED-Net.

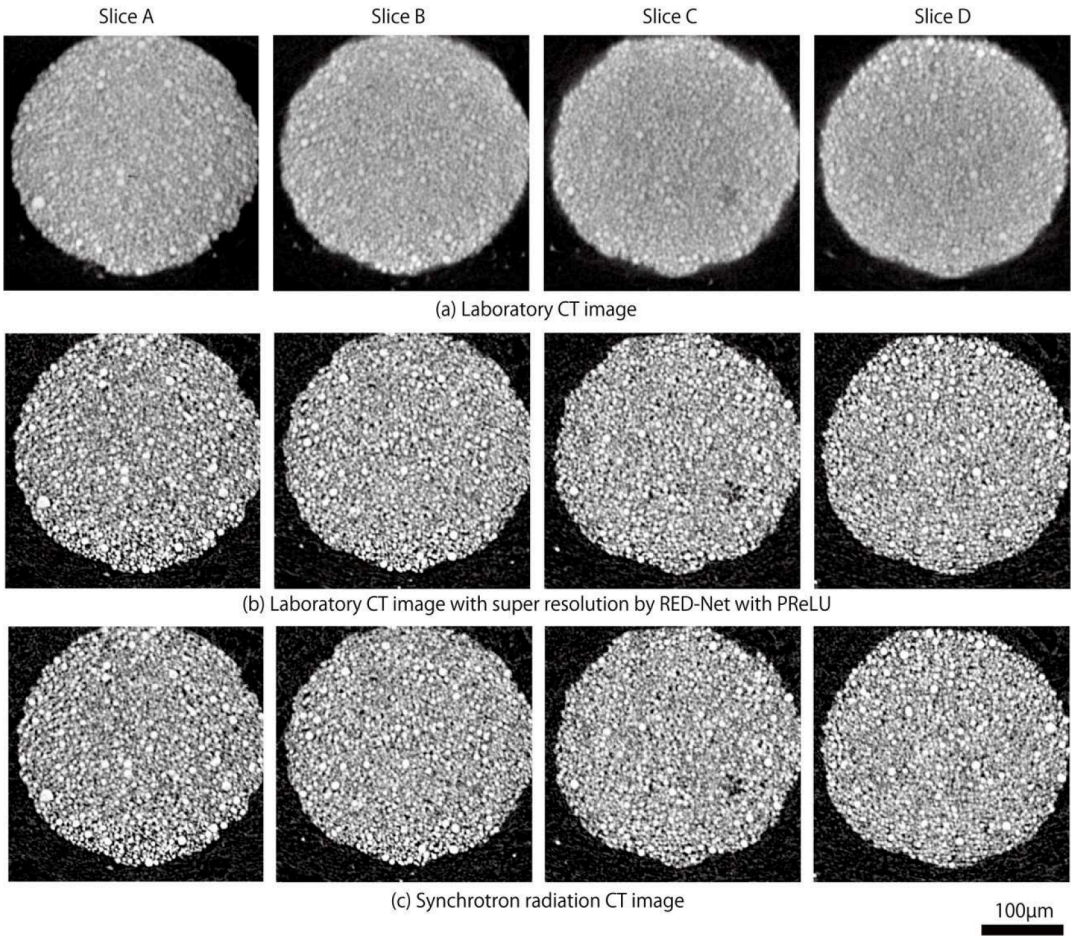

Fig. 8. Overall CT images: (a) laboratory CT image, (b) super-resolution processed laboratory CT image by RED-Net with PReLU, and (c) synchrotron radiation CT image.

characteristics of metal X-rays, resulting in relatively low resolution. Therefore, in this study, we attempted to achieve the super-resolution of laboratory X-ray CT images of all-solid-state batteries through machine learning using synchrotron radiation CT as the training data. The results show that the SRCNN is ineffective in achieving super-resolution with the present data because the feature extraction fails.

On the other hand, RED-Net successfully achieves super-resolution through effective feature extraction with the encoder and decoder networks. In addition, RED-Net produces a significant increase in PSNR when the PReLU activation function replaces the ReLU activation function. Applying PReLU to a six-layer RED-Net enables super-resolution of laboratory CT images with a PSNR of more than 30 dB to the synchrotron radiation CT image. As a result, high-resolution enhancement comparable to synchrotron radiation CT can be achieved with laboratory CT.

CRediT authorship contribution statement

M. Kodama: Writing – original draft, Methodology, Investigation. **A. Takeuchi:** Methodology, Resources. **M. Uesugi:** Methodology, Resources. **S. Hirai:** Project administration, Supervision.

Declaration of Competing Interest

The authors declare the following financial interests/personal relationships which may be considered as potential competing interests:

Manabu Kodama reports financial support was provided by Japan Keirin Autorace Foundation. MANABU KODAMA reports was provided by Japan Synchrotron Radiation Research Institute.

Data availability

Data will be made available on request.

Acknowledgments

Manabu Kodama acknowledges support from the Japan Keirin Autorace Foundation. The synchrotron radiation measurements were performed at BL20XU at SPring-8, with the approval of the Japan Synchrotron Radiation Research Institute (JASRI; proposal numbers 2022B1020, 2022A1003, 2021B1005, 2021B1004, 2021A1017, 2020A1782).

References

[1] Yong JY, Ramachandaramurthy VK, Tan KM, Mithulananthan N. A review on the state-of-the-art technologies of electric vehicle, its impacts and prospects. Renew Sustain Energy Rev 2015;49:365–85. https://doi.org/10.1016/j.rser.2015.04.130.
[2] Ramachandaramurthy VK, Ajmal AM, Kasinathan P, Tan KM, Yong JY, Vinoth R. Social acceptance and preference of EV users—a review. IEEE Access 2023;11:11956–72. https://doi.org/10.1109/ACCESS.2023.3241636.
[3] Weiss M, Ruess R, Kasnatscheew J, Levartovsky Y, Levy NR, Minnmann P, Stolz L, Waldmann T, Wohlfahrt-Mehrens M, Aurbach D, Winter M, Ein-Eli Y, Janek J. Fast charging of lithium-ion batteries: a review of materials aspects. Adv Energy Mater 2021;11:2101126. https://doi.org/10.1002/aenm.202101126.
[4] Qiu Y, Jiang F. A review on passive and active strategies of enhancing the safety of lithium-ion batteries. Int J Heat Mass Transf 2022;184:122288. https://doi.org/10.1016/j.ijheatmasstransfer.2021.122288.

[5] Lian PJ, Zhao BS, Zhang LQ, Xu N, Wu MT, Gao XP. Inorganic sulfide solid electrolytes for all-solid-state lithium secondary batteries. J Mater Chem A 2019;7:20540–57. https://doi.org/10.1039/C9TA04555D.
[6] Sakka Y, Yamashige H, Watanabe A, Takeuchi A, Uesugi M, Uesugi K, Orikasa Y. Pressure dependence on the three-dimensional structure of a composite electrode in an all-solid-state battery. J Mater Chem A 2022;10:16602–9. https://doi.org/10.1039/D2TA02378D.
[7] Iwamoto S, Kodama M, Yanagi K, Haniu Y, Fujii Y, Masuda N, Higuchi H, Suetsugu Y, Hirai S. Numerical simulations of all-solid-state batteries using specific contact area diameters for active materials determined by X-ray computed tomography. J Power Sources Adv 2023;21:100120. https://doi.org/10.1016/j.powera.2023.100120.
[8] So M, Inoue G, Hirate R, Nunoshita K, Ishikawa S, Tsuge Y. Effect of mold pressure on compaction and ion conductivity of all-solid-state batteries revealed by the discrete element method. J Power Sources 2021;508:230344. https://doi.org/10.1016/j.jpowsour.2021.230344.
[9] So M, Inoue G, Park K, Nunoshita K, Ishikawa S, Tsuge Y. Simulation of the compaction of an all-solid-state battery cathode with coated particles using the discrete element method. J Power Sources 2022;530:231279. https://doi.org/10.1016/j.jpowsour.2022.231279.
[10] So M, Yano S, Permatasari A, Pham TD, Park K, Inoue G. Mechanism of silicon fragmentation in all-solid-state battery evaluated by discrete element method. J Power Sources 2022;546:231956. https://doi.org/10.1016/j.jpowsour.2022.231956.
[11] Kashkooli AG, Farhad S, Lee DU, Feng K, Litster S, Babu SK, Zhu L, Chen Z. Multiscale modeling of lithium-ion battery electrodes based on nano-scale X-ray computed tomography. J Power Sources 2016;307:496–509. https://doi.org/10.1016/j.jpowsour.2015.12.134.
[12] Shi T, Zhang YQ, Tu Q, Wang Y, Scott MC, Ceder G. Characterization of mechanical degradation in an all-solid-state battery cathode. J Mater Chem A 2020;8:17399–404. https://doi.org/10.1039/D0TA06985J.
[13] Kodama M, Takeuchi A, Uesugi M, Miyuki T, Yasuda H, Hirai S. Nanoscale pore measurements in an all-solid-state lithium-ion battery with ultra-small-angle X-ray scattering (USAXS). J Power Sources Adv 2021;12:100076. https://doi.org/10.1016/j.powera.2021.100076.
[14] Kodama M, Komiyama S, Ohashi A, Horikawa N, Kawamura K, Hirai S. High-pressure in situ X-ray computed tomography and numerical simulation of sulfide solid electrolyte. J Power Sources 2020;462:228160. https://doi.org/10.1016/j.jpowsour.2020.228160.
[15] Kalender WA. X-ray computed tomography. Phys Med Biol 2006;51:R29–43. https://doi.org/10.1088/0031-9155/51/13/R03.
[16] Wang Y, Miller JD. Current developments and applications of micro-CT for the 3D analysis of multiphase mineral systems in geometallurgy. Earth Sci Rev 2020;211:103406. https://doi.org/10.1016/j.earscirev.2020.103406.
[17] Thompson AC, Llacer J, Campbell Finman L, Hughes EB, Otis JN, Wilson S, Zeman HD. Computed tomography using synchrotron radiation. Nucl Instrum Methods Phys Res 1984;222:319–23. https://doi.org/10.1016/0167-5087(84)90550-7.
[18] Uesugi K, Suzuki Y, Yagi N, Tsuchiyama A, Nakano T. Development of high spatial resolution X-ray CT system at BL47XU in SPring-8. Nucl Instrum Methods Phys Res Sect A Accel Spectrom Detect Assoc Equip 2001;467–468:853–6. https://doi.org/10.1016/S0168-9002(01)00491-0.
[19] B.A. Dowd, G.H. Campbell, R.B. Marr, V.V. Nagarkar, S.V. Tipnis, L. Axe, D.P. Siddons, Developments in synchrotron x-ray computed microtomography at the national synchrotron light source, in: U. Bonse (editor), Denver, CO, 1999: pp. 224–36. 10.1117/12.363725.
[20] Hosseini Dalasm NK, Kotaka T, Tabuchi Y, Pasaogullari U. A comparison of laboratory based and synchrotron based nano X-ray CT for PEFC micro porous layer. ECS Trans 2013;58:345–52. https://doi.org/10.1149/05801.0345ecst.
[21] Chen H, He X, Qing L, Wu Y, Ren C, Sheriff RE, Zhu C. Real-world single image super-resolution: a brief review. Inf Fusion 2022;79:124–45. https://doi.org/10.1016/j.inffus.2021.09.005.
[22] J. Shermeyer, A. Van Etten, The effects of super-resolution on object detection performance in satellite imagery, (2019). http://arxiv.org/abs/1812.04098.
[23] X.J. Mao, C. Shen, Y.B. Yang, Image restoration using very deep convolutional encoder-decoder networks with symmetric skip connections, (2016). http://arxiv.org/abs/1603.09056.
[24] Dreier T, Peruzzi N, Lundström U, Bech M. Improved resolution in x-ray tomography by super-resolution. Appl Opt 2021;60:5783. https://doi.org/10.1364/AO.427934.
[25] Omori T, Suzuki S, Michibayashi K, Okamoto A. Super-resolution of X-ray CT images of rock samples by sparse representation: applications to the complex texture of serpentinite. Sci Rep 2023;13:6648. https://doi.org/10.1038/s41598-023-33503-6.
[26] Mercier R, Malugani JP, Fahys B, Robert G. Superionic conduction in Li2S - P2S5 - LiI - glasses. Solid State Ion 1981;5:663–6. https://doi.org/10.1016/0167-2738(81)90341-6.
[27] Uesugi K, Takeuchi A, Suzuki Y. High-definition high-throughput micro-tomography at SPring-8. J Phys Conf Ser 2009;186:012050. https://doi.org/10.1088/1742-6596/186/1/012050.
[28] A.F. Agarap, Deep learning using Rectified Linear Units (ReLU), (2019). http://arxiv.org/abs/1803.08375.
[29] Shruthi KN, Shashank BM, Saketh YS, Prasantha HS, Sandya S. Comparison Analysis of a Biomedical Image for Compression Using Various Transform Coding Techniques. In: Proceedings of the IEEE 6th international conference on advanced computing (IACC). Bhimavaram, India: IEEE; 2016. p. 297–303. https://doi.org/10.1109/IACC.2016.63.
[30] A. Sasov, X. Liu, P.L. Salmon, Compensation of mechanical inaccuracies in micro-CT and nano-CT, in: S.R. Stock (editor), San Diego, California, USA, 2008: p. 70781C. 10.1117/12.793212.
[31] Kodama M, Ohashi A, Adachi H, Miyuki T, Takeuchi A, Yasutake M, Uesugi K, Kaburagi T, Hirai S. Three-dimensional structural measurement and material identification of an all-solid-state lithium-ion battery by X-Ray nanotomography and deep learning. J Power Sources Adv 2021;8:100048. https://doi.org/10.1016/j.powera.2021.100048.
[32] K. He, X. Zhang, S. Ren, J. Sun, Delving deep into rectifiers: surpassing human-level performance on ImageNet classification, (2015). http://arxiv.org/abs/1502.01852.